Continuum Mech. Thermodyn. (2021) 33:35–51
https://doi.org/10.1007/s00161-020-00884-2

ORIGINAL ARTICLE

A. Nischler · J. Denk · O. Huber

Fatigue modeling for wrought magnesium structures with various fatigue parameters and the concept of highly strained volume

Received: 16 December 2019 / Accepted: 30 March 2020 / Published online: 22 April 2020

Abstract Mechanical fatigue tests of unnotched, notched, and bending twin-roll cast AZ31B magnesium alloy specimens are performed in which strain fields are analyzed with digital image correlation. Clearly, delimited macroscopic bands of twinned grains (BTGs) in which the compressive strain is significantly higher compared to the adjacent regions are observed. Conventional fatigue parameters, e.g., the strain amplitude, exhibited higher values within the BTGs. This findings are confirmed by the fact that for all investigated specimens the initial macroscopic cracks are observed within the BTGs. Consequently, for the presented concept of highly strained volume, fatigue parameters are determined from the highly strained regions with high strain amplitudes. This paper focuses on the application of the effective strain amplitude fatigue parameter decomposed in an elastic and plastic portion, the Smith-Watson-Topper fatigue parameter and energy-based fatigue parameters within the concept of highly strained volume. An extended stress–strain hysteresis model is presented to compute stress–strain hystereses for arbitrary load ratios, required to determine the mentioned fatigue parameters. The application and evaluation of five different fatigue parameters within the concept of highly strained volume demonstrates the accurate description of the fatigue life until failure.

Keywords Wrought magnesium alloys · Fatigue modeling · Discontinuous strain field · Uniaxial stress–strain hysteresis model · Cyclic stress–strain curves

1 Introduction

Innovative materials for lightweight constructions, e.g., in the automotive industry, will become increasingly important in the future because they can contribute to reduce CO_2 emissions [18,22]. Magnesium (Mg) alloys are counted among these lightweight materials due to their excellent strength-to-weight ratio compared to conventional steel and aluminum alloys [18]. This work presents an approach for the fatigue modeling of cyclically loaded structural components made of the wrought AZ31B Mg alloy, as this is an important aspect in the design of lightweight components.

During the twin-roll cast process of Mg alloys at higher temperature, slip occurs predominantly on the basal planes, which leads to their alignment parallel to the direction of metal flow [2]. Consequently, a strong basal texture develops during the production, which means that most of the basal planes {0001} are approximately parallel to the sheet plane [21,29]. At ambient temperature, tensile stress in the sheet plane direction mainly activates basal $\langle a \rangle$ slip, whereas compressive stress leads to extensive $\{10\bar{1}2\}\langle 10\bar{1}1 \rangle$ tension twinning [2,5]. As a result of the basal texture and the dominant twin formation under compressive stress in the sheet plane

Communicated by Andreas Öchsner.

A. Nischler (✉) · J. Denk · O. Huber
Competence Center for Lightweight Design, Landshut University of Applied Sciences, Am Lurzenhof 1, 84036 Landshut, Germany
E-mail: anton.nischler@haw-landshut.de

directions, clearly delimited macroscopic bands of twinned grains (BTGs) are formed [5,8]. Within these BTGs, the compressive strain is considerably higher than outside the BTGs, leading to a discontinuous strain field [9]. In addition, [10] shows that common fatigue parameters such as strain amplitude, Smith–Watson–Topper or energy-based fatigue parameters, taken from inside BTGs, have higher values, which corresponds to the observation that the initial macroscopic crack is always within BTGs. Further challenges in fatigue modeling of basal textured wrought Mg alloys are anisotropic and asymmetric yield strengths, almost ideal plastic material behavior during twinning and sigmoidal shaped stress–strain hystereses [20,27,31].

In recent years, several works have been published on fatigue modeling, that deal with the complex deformation behavior of Mg alloys [5,19,23,26,27]. All these researches use a total strain energy density fatigue parameter, first introduced by Ellyin et al. [12]. Each work uses different approaches to determine the positive elastic strain energy density and achieves a good agreement between the predicted and experimental life for uniaxial unnotched specimens. Only a few investigations were carried out concerning the fatigue modeling of notched specimens [8,30,32], bending specimens [7,15,28] and the fatigue behavior under dominant multiaxial loading [1,24]. The mentioned researches investigate the influence of stress concentrations, stress gradients and different types of loading on fatigue life separately from each other and achieve good results in fatigue modeling for a specific specimen type (uniaxial unnotched specimen, notched specimen, bending specimen, axial and torsional loaded tubular specimen). Furthermore, the discontinuous strain field (BTGs), important for fatigue modeling [10], has not been taken into account by the mentioned researches.

To consider all these aspects in one fatigue model, Denk et al. [10] introduced the concept of highly strained volume (CHεV), inspired by the highly stressed volume from the early work of Kuguel [17]. They made in [10] fatigue tests on unnotched, notched and bending specimens and determined the size of the highly strained volume and the effective strain amplitude within the highly strained volume to predict the number of cycles to failure.

This work is an extension to [10], where further fatigue parameters such as the effective strain amplitude separated into an effective elastic and plastic strain amplitude, the Smith–Watson–Topper fatigue parameter and energy-based fatigue parameters are used. In addition, an extended stress–strain hysteresis model, based on Dallmeier et al. [4], is proposed that enables the computation of stress–strain hystereses of arbitrary load ratios required to calculate the mentioned fatigue parameters. Finally, the different fatigue parameters are evaluated and compared with each other.

2 Material and experimental procedure

The study for the fatigue tests was conducted with a commercial 3-mm-thick twin-roll cast AZ31B sheet with a strong basal texture. Detailed information on the microstructure of the tested material is given in [6]. Different types of unnotched uniaxial specimens, notched uniaxial specimens and unnotched bending specimens were tested with constant amplitude loading. Figure 1 and Table 1 show and list the geometrical dimensions of the different used specimens. Additionally, the stress concentration factors K_t of the notched uniaxial specimens are listed in Table 1. Further details on the specimen manufacturing can be found in [6].

The fatigue data for the unnotched uniaxial specimens were gathered strain-controlled with extensometer strain ratios $R_{\varepsilon,\mathrm{ext}} = 2, -\infty, -1, -0, 5$. In contrast, the notched uniaxial specimens and unnotched bending specimens were exclusively stress-controlled tested with the nominal stress ratios $R_{\sigma,\mathrm{n}} = -1, -0, 5$ and $R_{\sigma,\mathrm{n}} = -1$, respectively. An anti-buckling device is used to prevent the specimen from buckling when subjected to compressive stress. The in situ measured strain fields were obtained using the GOM ARAMIS™ 12M digital image correlation (DIC) photogrammetry system.

3 Proposed fatigue model

This section provides the theoretical approach for the concept of highly strained volume (CHεV) in combination with two effective strain amplitude fatigue parameters, the Smith–Watson–Topper fatigue parameter, and two energy density fatigue parameters. A uniaxial stress–strain hysteresis model is proposed to compute the stress–strain data required to determine four of a total of five fatigue parameters.

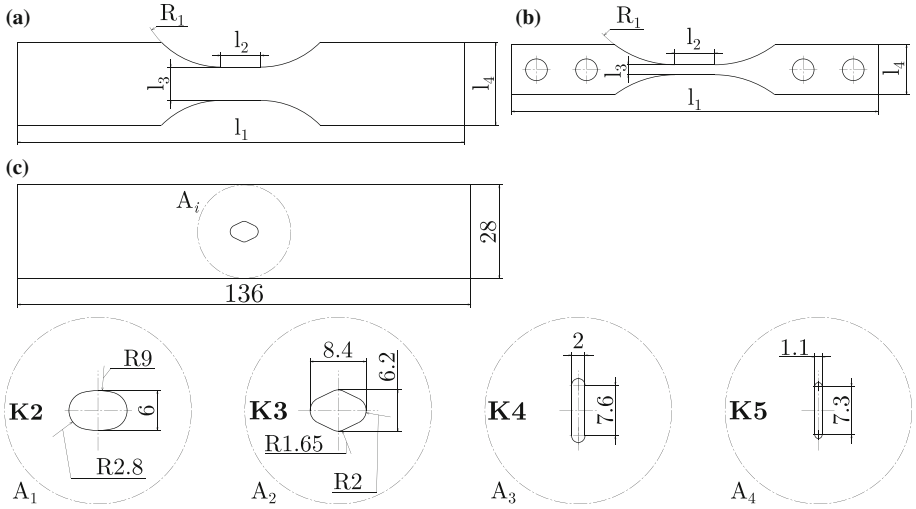

Fig. 1 Geometries of the different tested specimen types: **a** unnotched uniaxial specimens, **b** unnotched bending specimens and **c** notched uniaxial specimens for which the dimension are listed in Table 1. The four detail views A_i show the dimensions of the notch geometries K2, K3, K4, and K5

Table 1 Dimensions for the unnotched uniaxial and unnotched bending specimens as well as the stress concentration factors K_t for the notched uniaxial specimens

Unnotched uniaxial specimens	l_1 (mm)	l_2 (mm)	l_3 (mm)	l_4 (mm)	R_1 (mm)
T	100	6	3	15	25
S	100	15	5	15	25
M	134	12	10	25	25
L	110	30	7	15	25
H	130	60	10	25	25
Notched uniaxial specimens	Stress concentration factors K_t				
K2	1.86				
K3	3.14				
K4	4.26				
K5	5.48				
Unnotched bending specimens	l_1 (mm)	l_2 (mm)	l_3 (mm)	l_4 (mm)	R_1 (mm)
B30	110	12	3	15	30
B45	110	12	4.5	15	30
B60	110	12	6	15	30

3.1 The concept of highly strained volume

Figure 2a and b shows the components of the principal strain fields at the lower load level (LLL) $\varepsilon_3^*(x_1, x_2)|_{\mathrm{LLL}}$ and at the upper load level (ULL) $\varepsilon_1^*(x_1, x_2)|_{\mathrm{ULL}}$ at half of fatigue life $N_f/2$ for an unnotched uniaxial specimen. Note that the principal strains are sorted according to the convention $\varepsilon_1^* \geq \varepsilon_2^* \geq \varepsilon_3^*$ and that proportional cyclic loading is assumed. In the middle part of the specimen, the anti-buckling device covers the strain field.

Caused by the basal texture, the twin formation and the almost ideal plastic material behavior during twinning, a discontinuous strain field with macroscopic bands of twinned grains (BTG) is formed [9]. Figure 2a shows the resulting BTG in which the compressive strain is significantly higher (blue color) compared to the regions outside the BTG and the BTG is a clearly delimited subdomain. Its volume fraction, related to the gauge volume, is approximately 0.375. Figure 2b illustrates that even after a subsequent tensile load the BTG remains in place and shows still a compressive strain.

The investigations revealed that initial macroscopic cracks are always located within the BTG [9], as it can be seen in the image detail of Fig. 2b. It should be noted that the image detail in Fig. 2b is taken from this position, but at a later stage. The red stripe indicates a large measured tensile strain, which results from an opening crack. This finding can be explained with the help of Fig. 3, which shows stress–strain hystereses (SSH) obtained via DIC at certain strain increments from inside and outside the BTG. The normal strain

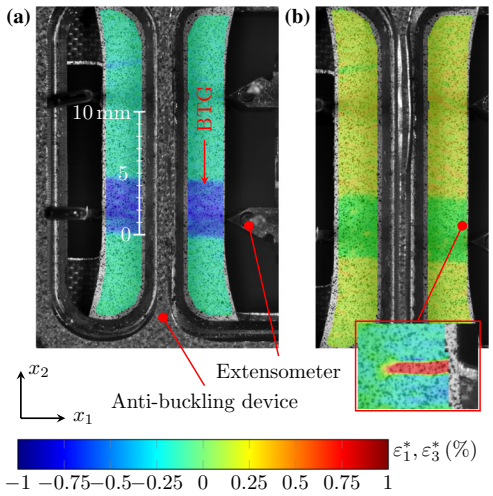

Fig. 2 Principal strain fields $\varepsilon_{ij}^*(x_1, x_2)$ of an unnotched specimen at half of fatigue life $N_f/2$ with a extensometer strain amplitude $\varepsilon_{a,ext} = 0.35\%$ and an extensometer strain ratio $R_{\varepsilon,ext} = -1$ measured with DIC: **a** principal strain field at the lower load level $\varepsilon_3^*(x_1, x_2)|_{LLL}$ with the marked BTG, **b** principal strain field at the upper load level $\varepsilon_1^*(x_1, x_2)|_{ULL}$ with an image detail indicating that the macroscopic crack starts within the BTG. The image detail is taken from the marked position, but at N_f

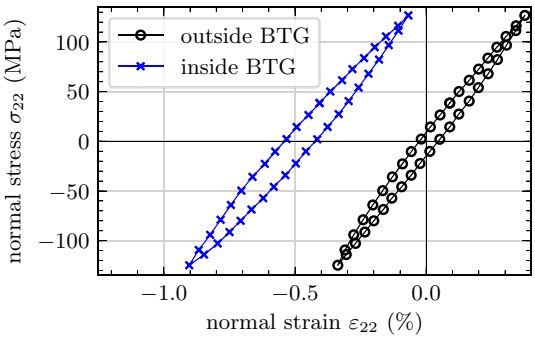

Fig. 3 stress–strain hystereses at half of fatigue life $N_f/2$ outside and inside the BTG measured incrementally with DIC from the uniaxial specimen shown in Fig. 2 with the corresponding coordinate system. For the normal strains ε_{22} outside and inside the BTG, the mean values of the respective normal strain fields $\varepsilon_{22}(x_1, x_2)$ are calculated

$\varepsilon_{22} = \frac{\partial u_2}{\partial x_2}$ refer to the coordinate system of Fig. 2, and thus means the normal strain in the x_2 direction. Inside the BTG, the total strain amplitude of the SSH is 17% and the hysteresis area is 70% larger compared to the SSH outside the BTG. Hence all of the common fatigue parameters like the strain amplitude, the Smith–Watson–Topper fatigue parameter and an energy density-based fatigue parameter are higher within the BTG. Since the extensometer strain amplitude $\varepsilon_{a,ext} = 0.35\%$ is small, the stress–strain hystereses in Fig. 3 do not have distinct sigomidal shapes.

In summary, the strongly discontinuous strain field and the higher fatigue parameter values within BTGs are the main motivation for using the CHεV [10]. Figure 4 illustrates the separation of the highly strained region (HSR) from a general strain field $\varepsilon_{ij}(x_1, x_2)|_{LLL}$ at the LLL. Starting with the components of a general strain tensor $\varepsilon_{ij}(x_1, x_2)|_{LLL}$, the components of the principal strain field $\varepsilon_{ij}^*(x_1, x_2)$ and the corresponding transformation matrix $a_{ij}^*(x_1, x_2)|_{LLL}$ have to be calculated. Furthermore, the maximum $\varepsilon_{1,max}^*|_{LLL}$ and the minimum value $\varepsilon_{3,min}^*|_{LLL}$ of the entire principal strain field at the LLL $\varepsilon_{ij}^*(x_1, x_2)|_{LLL}$ are determined. Subsequently, the HSR is separated using a threshold strain

$$\varepsilon_{thr}|_{LLL} = \begin{cases} 0.8\,\varepsilon_{1,max}^*|_{LLL}, & \text{if } |\varepsilon_{1,max}^*|_{LLL}| \geqslant |\varepsilon_{3,min}^*|_{LLL}| \\ 0.8\,\varepsilon_{3,min}^*|_{LLL}, & \text{if } |\varepsilon_{3,min}^*|_{LLL}| > |\varepsilon_{1,max}^*|_{LLL}|\,. \end{cases} \tag{1}$$

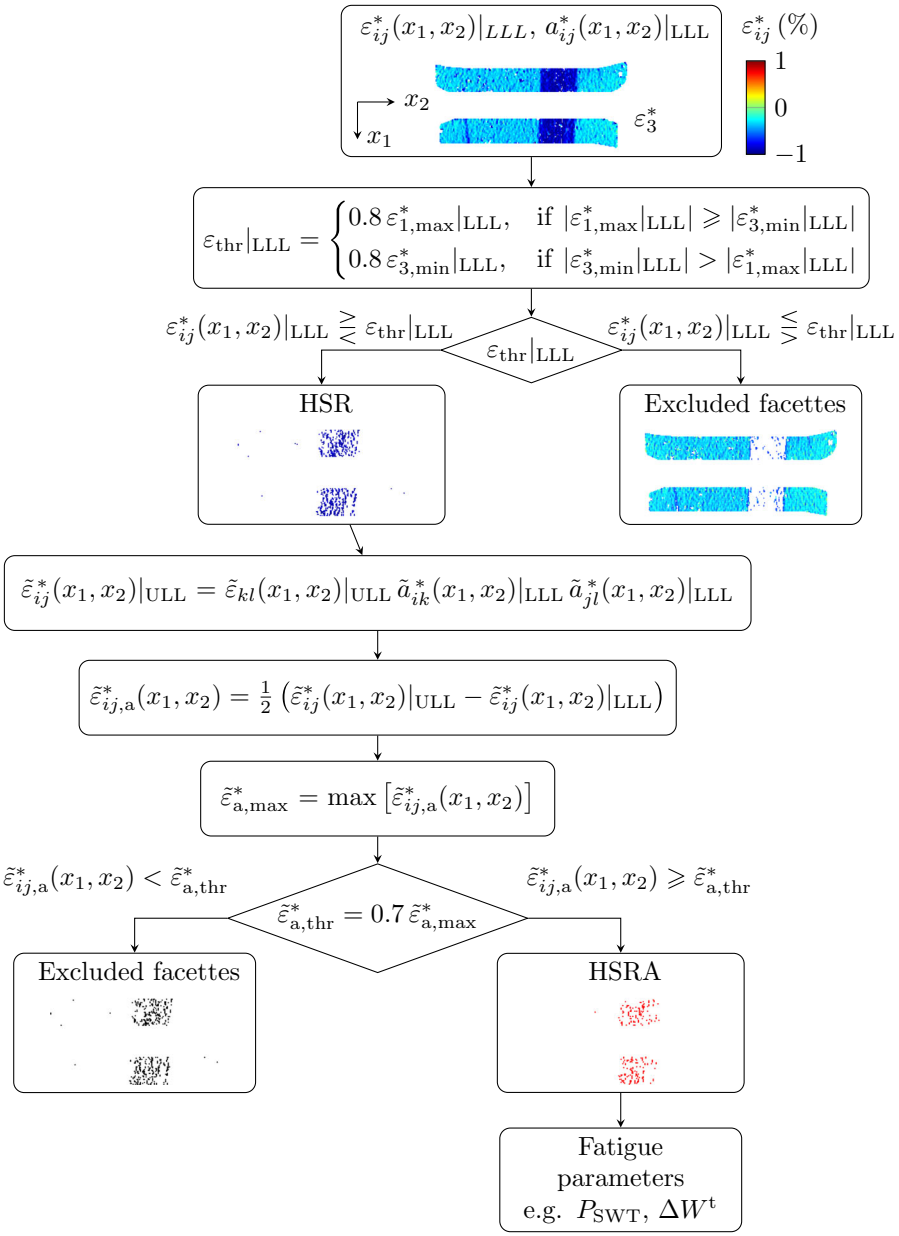

Fig. 4 Procedure for determining the HSR and subsequently the HSRA, based on the measured strain field $\varepsilon^*_{ij}(x_1, x_2)$ at the lower and upper load level with DIC of a uniaxial unnotched specimen

Best results for fatigue modeling are achieved by determining the HSR with the principal strain field $\varepsilon^*_{ij}(x_1, x_2)$ and a threshold value of $0.8\,\varepsilon^*_{1,\max}|_{\mathrm{LLL}}$ or $0.8\,\varepsilon^*_{3,\min}|_{\mathrm{LLL}}$ [6]. Further evaluation procedures for the HSR, such as different threshold values, are described in [6]. All of the strain fields are evaluated at $N_{\mathrm{f}}/2$ since a stabilized material behavior is achieved [9]. Figure 3 shows the separated HSR that meets $\varepsilon^*_{ij}(x_1, x_2)|_{\mathrm{LLL}} \gtrless \varepsilon_{\mathrm{thr}}|_{\mathrm{LLL}}$, which predominantly originates from the BTG. For the remaining principal strain field at the upper load level (ULL) $\varepsilon^*_{ij}(x_1, x_2)|_{\mathrm{ULL}}$, the same measuring facettes k are used as for the selected HSR.

A high compressive strain does not necessarily cause material failure. In contrast, the strain amplitude has a significant influence on the fatigue lifetime. Therefore, the effective strain amplitude tensors

$$\tilde{\varepsilon}^*_{ij,\mathrm{a}}(x_1, x_2) = \frac{1}{2}\left(\tilde{\varepsilon}^*_{ij}(x_1, x_2)|_{\mathrm{ULL}} - \tilde{\varepsilon}^*_{ij}(x_1, x_2)|_{\mathrm{LLL}}\right) \tag{2}$$

are calculated from the separated HSR, whereby effective quantities from the HSR are indicated with ($\tilde{\blacksquare}$). To ensure that the coordinate systems of $\tilde{\varepsilon}^*_{ij}(x_1, x_2)|_{\mathrm{ULL}}$ and $\tilde{\varepsilon}^*_{ij}(x_1, x_2)|_{\mathrm{LLL}}$ have the same orientation, a transformation

$$\tilde{\varepsilon}^*_{ij}(x_1, x_2)|_{\mathrm{ULL}} = \tilde{\varepsilon}_{kl}(x_1, x_2)|_{\mathrm{ULL}}\, \tilde{a}^*_{ik}(x_1, x_2)|_{\mathrm{LLL}}\, \tilde{a}^*_{jl}(x_1, x_2)|_{\mathrm{LLL}} \tag{3}$$

of the components of the effective strain tensor $\tilde{\varepsilon}_{kl}(x_1, x_2)|_{\mathrm{ULL}}$ is performed and $\tilde{\varepsilon}^*_{ij}(x_1, x_2)|_{\mathrm{ULL}}$ is used in Eq. 2. The components of $\tilde{\varepsilon}^*_{ij}(x_1, x_2)|_{\mathrm{ULL}}$ are not sorted according to the convention $\tilde{\varepsilon}^*_1|_{\mathrm{ULL}} \geq \tilde{\varepsilon}^*_2|_{\mathrm{ULL}} \geq \tilde{\varepsilon}^*_3|_{\mathrm{ULL}}$, otherwise the wrong components are subtracted in Eq. 2. The highly strained region with high strain amplitudes (HSRA) is separated by defining a threshold strain amplitude

$$\tilde{\varepsilon}^*_{\mathrm{a,thr}} = 0.7\, \tilde{\varepsilon}^*_{\mathrm{a,max}}\,, \tag{4}$$

with the maximum effective principal strain amplitude component

$$\tilde{\varepsilon}^*_{\mathrm{a,max}} = \max\left[\tilde{\varepsilon}^*_{ij,\mathrm{a}}(x_1, x_2)\right] \tag{5}$$

of the entire strain field. The definition of the threshold strain amplitude $\tilde{\varepsilon}^*_{\mathrm{a,thr}}$ ensures that only those regions are selected for the HSRA that are not only twinned but also untwinned after load reversal. This was determined by analyzing strain fields and micrographs [6]. Additionally, good fatigue modeling results were obtained with a threshold strain amplitude $\tilde{\varepsilon}^*_{\mathrm{a,thr}}$ of 70% of the maximum effective principal strain amplitude component $\tilde{\varepsilon}^*_{\mathrm{a,max}}$. Figure 3 shows the HSRA remaining at the end of the calculation algorithm, which is further used to determine fatigue parameters, such as the highly strained volume V_ε.

3.2 Fatigue parameters

Highly strained volume V_ε The highly strained volume V_ε is determined from the HSRA and the sheet thickness t. For this purpose, the highly strained area A_ε is calculated, which is the sum of the areas A_k for all measuring facettes k that are included in the HSRA. By multiplying the highly strained area A_ε and the measured specimen thickness t, the highly strained volume V_ε is calculated with the equation

$$V_\varepsilon = \sum_{k=1}^{n} A_k\, t\,. \tag{6}$$

Its size depends on the current load and on the specimen geometry. A large highly strained volume V_ε leads to smaller numbers of cycles to failure N_f and vice versa. By defining V_ε as an absolute quantity, geometric size effects, stress gradients and stress concentrations are considered with the fatigue model CHεV. For the unnotched specimens, the minimum and maximum measured highly strained volumes are $V_{\varepsilon,\mathrm{min}} = 0.97\mathrm{mm}^3$ and $V_{\varepsilon,\mathrm{max}} = 864\mathrm{mm}^3$, respectively. The notched specimens have values between $V_{\varepsilon,\mathrm{min}} = 0.192\mathrm{mm}^3$ and $V_{\varepsilon,\mathrm{max}} = 20.6\mathrm{mm}^3$ and the values for the bending specimens are between $V_{\varepsilon,\mathrm{min}} = 0.579\mathrm{mm}^3$ and $V_{\varepsilon,\mathrm{max}} = 9.3\mathrm{mm}^3$.

Fatigue parameters representing the load In the following, the used fatigue parameters in combination with the CHεV are explained. The different measuring facettes k of the HSRA have different effective principal strain amplitudes $\tilde{\varepsilon}^*_{\mathrm{a},k}$. Thus, a mean value is calculated yielding a unique scalar value for the strain amplitude within the HSRA. Accordingly, the maximum arithmetic mean effective principal strain amplitude is calculated by

$$\tilde{\bar{\varepsilon}}^*_\mathrm{a} = \max\left[\frac{1}{n}\sum_{k=1}^{n}\tilde{\varepsilon}^*_{ij,\mathrm{a},k}\right]. \tag{7}$$

Quantities marked with ($\tilde{\bar{\blacksquare}}$) represent mean effective measured values within the HSR or HSRA. In addition, the corresponding mean effective strain ratio is calculated by

$$\tilde{\bar{R}}_\varepsilon = \frac{\sum_{k=1}^{n}\tilde{\varepsilon}^*_k(x_1, x_2)|_{\mathrm{LLL}}}{\sum_{k=1}^{n}\tilde{\varepsilon}^*_k(x_1, x_2)|_{\mathrm{ULL}}} \tag{8}$$

which describes the actual effective strain ratio within the HSRA. In Eq. (8), the same component is used for the effective principal strains $\tilde{\varepsilon}_k^*(x_1, x_2)|_{\mathrm{LLL}}$ and $\tilde{\varepsilon}_k^*(x_1, x_2)|_{\mathrm{ULL}}$, which is derived from the calculation of the maximum arithmetic mean effective principal strain amplitude $\tilde{\bar{\varepsilon}}_{\mathrm{a}}^*$ in Eq. (7). The mean effective principal strain amplitude $\tilde{\bar{\varepsilon}}_{\mathrm{a}}^*$ in Eq. (7) is the only investigated fatigue parameter that does not require knowledge of the stress state.

Another fatigue parameter is the decomposed mean effective principal strain amplitude $\tilde{\bar{\varepsilon}}_{\mathrm{a}}^*$, represented by an elastic $\tilde{\bar{\varepsilon}}_{\mathrm{a}}^{*,\mathrm{el}}$ and a plastic $\tilde{\bar{\varepsilon}}_{\mathrm{a}}^{*,\mathrm{pl}}$ portion which is calculated by

$$\tilde{\bar{\varepsilon}}_{\mathrm{a}}^* = \tilde{\bar{\varepsilon}}_{\mathrm{a}}^{*,\mathrm{el}} + \tilde{\bar{\varepsilon}}_{\mathrm{a}}^{*,\mathrm{pl}} = \frac{\tilde{\sigma}_{\mathrm{a}}^*}{E} + \tilde{\bar{\varepsilon}}_{\mathrm{a}}^{*,\mathrm{pl}} \tag{9}$$

with the effective principal stress amplitude $\tilde{\sigma}_{\mathrm{a}}^*$ and the Young's modulus E. Another analyzed fatigue parameter is the Smith–Watson–Topper fatigue parameter P_{SWT} that takes into account the influence of the effective mean principal stress $\tilde{\sigma}_{\mathrm{m}}^*$. It is defined by

$$P_{\mathrm{SWT}} = \sqrt{\left(\tilde{\sigma}_{\mathrm{m}}^* + \tilde{\sigma}_{\mathrm{a}}^*\right) \tilde{\bar{\varepsilon}}_{\mathrm{a}}^* \, E}\,, \tag{10}$$

wherein the mean effective principal strain amplitude $\tilde{\bar{\varepsilon}}_{\mathrm{a}}^*$ is calculated with Eq. (7).

Additionally, the total strain energy density fatigue parameter, introduced in [13], is calculated with

$$\Delta W^{\mathrm{t}} = \Delta W^{+\mathrm{el}} + \Delta W^{\mathrm{pl}} \tag{11}$$

and used within this paper. The total strain energy density is defined as the positive elastic strain energy density $\Delta W^{+\mathrm{el}}$ and the plastic strain energy density ΔW^{pl}. Among the different calculation methods for the positive elastic strain energy density [5,16,19,27], the equations

$$\Delta W^{+\mathrm{el}} = \begin{cases} \frac{\tilde{\sigma}^*{}_{\mathrm{max}}^{\,2}}{2E}, & \text{if } \tilde{\sigma}_{\mathrm{min}}^* \leq 0 \\ \frac{\tilde{\sigma}^*{}_{\mathrm{max}}^{\,2} - \tilde{\sigma}^*{}_{\mathrm{min}}^{\,2}}{2E}, & \text{if } \tilde{\sigma}_{\mathrm{min}}^* > 0\,, \end{cases} \tag{12}$$

according to [5], are used here. In Eq. 12, $\tilde{\sigma}_{\mathrm{max}}^*$ and $\tilde{\sigma}_{\mathrm{min}}^*$ are the effective maximum and minimum principal stress at the upper and lower load level within the HSRA. A variant of the total strain energy density ΔW^{t} for AZ31B Mg alloy is the total strain energy density with a mean stress sensitivity factor $f_{\mathrm{mss}} = 0.25$ from [5], resulting in

$$\Delta W_{\mathrm{mss}}^{\mathrm{t}} = f_{\mathrm{mss}}\, \Delta W^{+\mathrm{el}} + \Delta W^{\mathrm{pl}}\,, \tag{13}$$

in which f_{mss} adjusts the influence of the mean stress.

It should be noted that for the fatigue parameter $\tilde{\bar{\varepsilon}}_{\mathrm{a}}^{*,\mathrm{el}} + \tilde{\bar{\varepsilon}}_{\mathrm{a}}^{*,\mathrm{pl}}$ in Eq. (9), P_{SWT} in Eq. (10), ΔW^{t} in Eq. (11) and $\Delta W_{\mathrm{mss}}^{\mathrm{t}}$ in Eq. (13) stress–strain hystereses must be determined and therefore the stress state must be known. It is demonstrated in [9] that the discontinuous strain field illustrated in Fig. 2 cannot be calculated with current phenomenological material models such as the Cazacu, Plunket and Barlat yield criterion CPB06 [3]. Hence, for that lack of an accurate 2D and 3D material model, a phenomenological uniaxial stress–strain hysteresis model was developed [4], which is explained in detail in the next section.

3.3 Extended stress–strain hysteresis model

This section describes the phenomenological uniaxial stress–strain hysteresis model used for calculating fatigue parameters. Dallmeier et al. published in [4] a basic stress–strain hysteresis model (SSM), which gives accurate results for a load ratio of $R_\varepsilon = -1$. In the following, the most important equations as well as an extension of the SSM for $R_\varepsilon \neq -1$ are shown.

Basic stress–strain hysteresis model Conventional functions for nonlinear stress–strain relationship, such as the Ramberg–Osgood equation, are improper due to the distinct asymmetry between the tensile and compressive yield strength and the sigmoidal shaped stress–strain curves, mainly caused by twinning and detwinning [20,25,31]. Therefore, the approach

$$\Delta\varepsilon^{\mathrm{t}}(\Delta\sigma) = \Delta\varepsilon^{\mathrm{el}}(\Delta\sigma) + \Delta\varepsilon^{\mathrm{psel}}(\Delta\sigma) + \Delta\varepsilon^{\mathrm{pl}}(\Delta\sigma) \tag{14}$$

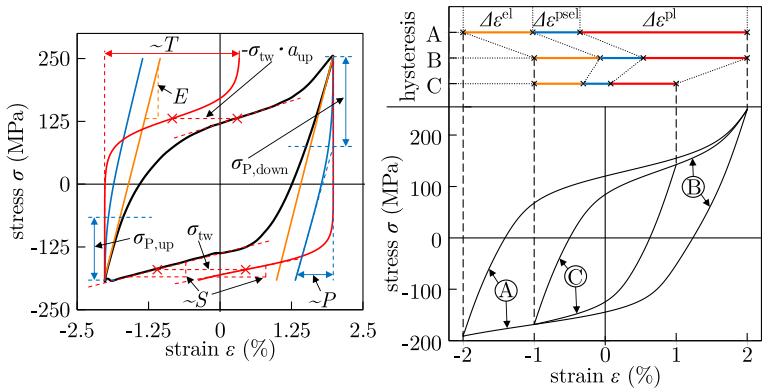

Fig. 5 Explanation of the: **a** material parameters used to calculate the elastic $\Delta\varepsilon^{\mathrm{el}}(\Delta\sigma)$ (orange curve), plastic $\Delta\varepsilon^{\mathrm{pl}}(\Delta\sigma)$ (red curve) and pseudoelastic $\Delta\varepsilon^{\mathrm{psel}}(\Delta\sigma)$ (blue curve) strain increment for the calculation of the measured stress–strain hysteresis (black curve), **b** composition of the elastic strain increment $\Delta\varepsilon^{\mathrm{el}}(\Delta\sigma)$, the plastic strain increment $\Delta\varepsilon^{\mathrm{pl}}(\Delta\sigma)$ (red curve) and the pseudoelastic strain increment $\Delta\varepsilon^{\mathrm{psel}}(\Delta\sigma)$ (blue curve) using the example of an envelop stress–strain hysteresis with two inner hystereses. [4]

describes the total strain increment $\Delta\varepsilon^{\mathrm{t}}(\Delta\sigma)$, which consists of an elastic $\Delta\varepsilon^{\mathrm{el}}(\Delta\sigma)$, a pseudoelastic $\Delta\varepsilon^{\mathrm{psel}}(\Delta\sigma)$ and a plastic strain increment $\Delta\varepsilon^{\mathrm{pl}}(\Delta\sigma)$ as illustrated in Fig. 5a and b. The measured mean effective strain values of the HSRA at the upper $\tilde{\bar{\varepsilon}}|_{\mathrm{ULL}}$ and lower load levels $\tilde{\bar{\varepsilon}}|_{\mathrm{LLL}}$ are used as input values for the hysteresis model. The elastic strain increment as a function of the stress increment $\Delta\sigma$ is

$$\Delta\varepsilon^{\mathrm{el}}(\Delta\sigma) = \frac{\Delta\sigma}{E}\,. \tag{15}$$

For the plastic deformation, caused by twinning and de-twinning, the equation

$$\Delta\varepsilon^{\mathrm{pl}}(\Delta\sigma) = \left[U(\Delta\sigma) - U(\Delta\sigma = 0)\right]\, T\, m^{\mathrm{pl}} \tag{16}$$

is given, where the coefficient T describes twice the amount of the plastic strain at the inflection point of $\Delta\varepsilon^{\mathrm{pl}}(\Delta\sigma)$ (Fig. 5a) and the memory factor m^{pl} which ensure material memory [4]. The substituent $U(\Delta\sigma)$ is

$$U(\Delta\sigma) = \frac{1}{2}\left[\tanh\left[\frac{\Delta\sigma - |\sigma_{\mathrm{rp}}| + a_{\mathrm{up/down}}\,\sigma_{\mathrm{tw}}}{S}\,a_{\mathrm{up/down}}\right] + 1\right] \tag{17}$$

and gives the stress–strain curve its sigmoidal shape through the tanh function. In Eq. (17), σ_{rp} is the stress at the reversal point at the beginning of the current stress–strain branch, σ_{tw} is the stress and S the slope at the inflection point of $\Delta\varepsilon^{\mathrm{pl}}(\Delta\sigma)$. For the factor $a_{\mathrm{up,down}}$, a distinction must be made between the following two cases

$$a_{\mathrm{up/down}} = \begin{cases} \frac{1}{2}\left[\tanh\left[\frac{\Delta\sigma - |\sigma_{\mathrm{rp}}| + \sigma_{\mathrm{tw}}}{S}\right] + 1\right], & \text{if } \Delta\varepsilon^{\mathrm{t}} > 0 \\ 1, & \text{if } \Delta\varepsilon^{\mathrm{t}} < 0\,, \end{cases} \tag{18}$$

in which $\Delta\varepsilon^{\mathrm{t}} > 0$ indicates an ascending stress–strain branch and $\Delta\varepsilon^{\mathrm{t}} < 0$ a descending stress–strain branch. The pseudoelastic portion is defined as

$$\Delta\varepsilon^{\mathrm{psel}}(\Delta\sigma) = \ln\left[\frac{\exp^{\Delta\sigma - \sigma_{\mathrm{P,up/down}}/50\,\mathrm{MPa}} + 1}{\exp^{-\sigma_{\mathrm{P,up/down}}/50\,\mathrm{MPa}} + 1}\right] P\, m^{\mathrm{psel}} \tag{19}$$

with the slope P of the pseudoelastic strain increment $\Delta\varepsilon^{\mathrm{psel}}(\Delta\sigma)$, the pseudoelastic cutoff stress $\sigma_{\mathrm{P,up/down}}$ for ascending and descending stress–strain reversals and the memory factor m^{psel}. The material parameters E, T, σ_{tw}, S, P, $\sigma_{\mathrm{P,up}}$ and $\sigma_{\mathrm{P,down}}$ are illustrated in Fig. 5a. The used material parameter values within this work

Table 2 Material parameters used for the phenomenological stress–strain hysteresis model for 3-mm-thick twin-roll cast AZ31B sheet metal

Material parameter	Value	Material parameter	Value
E	44200 MPa	P	0.0015
T	0.06	$\sigma_{P,\mathrm{up}}$	155 MPa
σ_{tw}	− 160 MPa	$\sigma_{P,\mathrm{down}}$	165 MPa
S	40 MPa	R_{r}	0.3

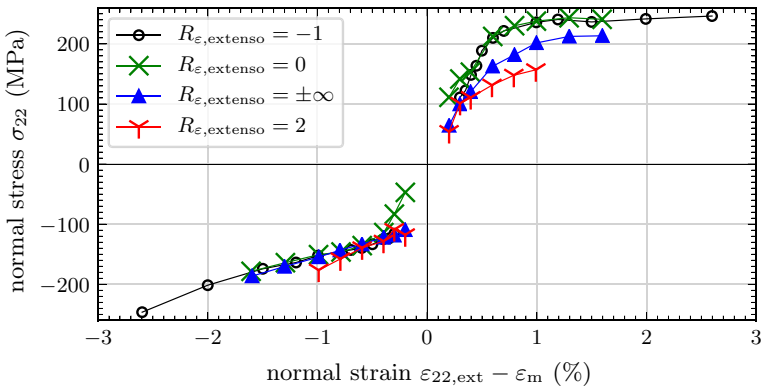

Fig. 6 Cyclic stress–strain curves (CSSCs) for the extensometer strain ratios $R_{\varepsilon,\mathrm{ext}} = -1,\ 2,\ \pm\infty$ and 0 with the mean strain ε_{m} being subtracted from the normal strain $\varepsilon_{22,\mathrm{ext}}$

are listed in Table 2. The memory factors m^{pl} and m^{psel} ensure closed hysteresis loops and are determinable after the first hysteresis branch has been calculated. Thus, the additional parameter

$$R_{\mathrm{r}} = \frac{1 - m^{\mathrm{psel}}}{1 - m^{\mathrm{pl}}} \tag{20}$$

applies for the first branch and defines how much strain is achieved by $\Delta\varepsilon^{\mathrm{pl}}(\Delta\sigma)$ and $\Delta\varepsilon^{\mathrm{psel}}(\Delta\sigma)$. The definition and the computation of the memory factors m^{pl} and m^{psel} as well as a detailed description of the basic SSM can be found in [4].

Extended stress–strain hysteresis model for arbitrary load ratios As shown in Fig. 3, the effective strain ratio $\tilde{R}_{\varepsilon}$ within the BTG differs significantly from the controlled extensometer strain ratio $R_{\varepsilon,\mathrm{ext}}$. Consequently, an extension for the basic SSM is necessary to calculate hystereses for arbitrary load ratios. For this purpose, the cyclic stress–strain curves (CSSCs) for strain ratios $R_{\varepsilon,\mathrm{ext}} = 2, \pm\infty$ and 0 are determined experimentally with 3-mm-thick wrought AZ31B uniaxial specimens and included into the SSM additionally to the CSSC for the strain ratio $R_{\varepsilon,\mathrm{ext}} = -1$. The CSSCs result from the maximum and minimum stress–strain values measured at the upper and lower load levels of the cyclically stable stress–strain hystereses at $N_{\mathrm{f}}/2$. Figure 6 illustrates the determined CSSCs for the different strain ratios, wherein the extensometer strain $\varepsilon_{22,\mathrm{ext}}$ is shifted by the mean strain ε_{m} in order to compare them more easily.

To minimize the experimental effort, only four strain ratios are determined. However, any strain ratio can occur in the BTG. Thus, the CSSCs are interpolated using a weighting coefficient W_{R} for arbitrary strain ratios. The value range of the weighting coefficient is $0 \leq W_{\mathrm{R}} \leq 1$, in which the weighting coefficient is 0 for the first adjacent cyclic stress–strain curve CSSC_1 and 1 for the second adjacent cyclic stress–strain curve CSSC_2.

In between, it is determined for the different strain ratio ranges R_ε as follows

$$W_\mathrm{R} = \begin{cases} \dfrac{\left(\tilde{\bar{\varepsilon}}|_\mathrm{ULL} - \tilde{\bar{\varepsilon}}|_\mathrm{LLL} \Big/ 2\right)}{|\tilde{\bar{\varepsilon}}|_\mathrm{LLL}/2|}, & 2 < R_\varepsilon < +\infty \quad (21) \\ \dfrac{\tilde{\bar{\varepsilon}}|_\mathrm{ULL}}{|\tilde{\bar{\varepsilon}}|_\mathrm{LLL}|}, & -\infty < R_\varepsilon < -1 \quad (22) \\ \dfrac{\tilde{\bar{\varepsilon}}|_\mathrm{ULL} - |\tilde{\bar{\varepsilon}}|_\mathrm{LLL}|}{|\tilde{\bar{\varepsilon}}|_\mathrm{ULL}|}, & -1 < R_\varepsilon < 0\,. \quad (23) \end{cases}$$

As an example, if the strain ratio is $R_\varepsilon = 3$, the value lies between the strain ratios $R_\varepsilon = 2$ and $R_\varepsilon = \pm\infty$ for which the CSSCs are measured experimentally. The first adjacent cyclic stress–strain curve CSSC_1 would thus be the one with the strain ratio $R_\varepsilon = 2$ and the second adjacent cyclic stress–strain curve CSSC_2 the one with the strain ratio $R_\varepsilon = \pm\infty$. In this case, the weighting coefficient W_R can be calculated with Eq. (21).

It should be mentioned that the mean effective strains at the upper and lower load levels $\tilde{\bar{\varepsilon}}|_\mathrm{ULL}$ and $\tilde{\bar{\varepsilon}}|_\mathrm{LLL}$, used in Eqs. (21), (22) and (23), are known from the experimentally measured strain fields. The associated maximum and minimum stresses σ_max and σ_min are then determined with the extended SSM. Accordingly, the maximum stress for the SSH can be calculated with

$$\sigma_\mathrm{max} = (1 - W_\mathrm{R})\ \sigma_\mathrm{max}|_{\mathrm{CSSC}_1} + W_\mathrm{R}\ \sigma_\mathrm{max}|_{\mathrm{CSSC}_2} \quad (24)$$

and the minimum stress for the SSH with

$$\sigma_\mathrm{min} = (1 - W_\mathrm{R})\ \sigma_\mathrm{min}|_{\mathrm{CSSC}_1} + W_\mathrm{R}\ \sigma_\mathrm{min}|_{\mathrm{CSSC}_2}\,. \quad (25)$$

Model verification To verify the extended SSM, stress–strain hystereses within the BTGs are experimentally determined for four uniaxial specimens and compared with the numerically calculated stress–strain hystereses, which is illustrated in Fig. 7. For the experiment, the strain field is measured with DIC and the mean effective normal strain $\tilde{\bar{\varepsilon}}_{22}$ within the HSR is determined. The normal stress σ_{22} is calculated by dividing the measured force by the measured specimen cross-sectional area. According to Fig. 7a and b, the measured and numerically simulated stress–strain hystereses are in good agreement with each other. To evaluate the extended SSM quantitatively, the ratios between the experimentally measured and numerically calculated maximum stresses σ_max, stress amplitudes σ_a, elastic $\Delta W^{+\mathrm{el}}$ and plastic strain energy densities ΔW^pl are calculated. These results, for different mean effective strain ratios $\tilde{\bar{R}}_\varepsilon$, are listed in Table 3.

The results show that the simulated maximum stresses and stress amplitudes have a maximum deviation of 7% from the experimental values. Furthermore, the ratios of the positive elastic strain energy density $\Delta W^{+\mathrm{el}}|_\mathrm{exp}/\Delta W^{+\mathrm{el}}|_\mathrm{sim}$ are acceptable with a maximum deviation of 15%. The largest deviations are obtained for the plastic strain energy density ratios $\Delta W^\mathrm{pl}|_\mathrm{exp}/\Delta W^\mathrm{pl}|_\mathrm{sim}$, with a maximum deviation of 28.9%.

4 Results and discussion

In this section, the CHεV is applied to the uniaxial unnotched, uniaxial notched and the bending specimens. Additionally, the CHεV is applied to each specimen type separately. For all shown results, the HSR and HSRA are evaluated with the criteria according to Eqs. (1) and Eq.4). The fatigue parameters $\tilde{\bar{\varepsilon}}_\mathrm{a}^*$, $\tilde{\bar{\varepsilon}}_\mathrm{a}^{*,\mathrm{el}} + \tilde{\bar{\varepsilon}}_\mathrm{a}^{*,\mathrm{pl}}$, P_SWT, ΔW^t and $\Delta W^\mathrm{t}_\mathrm{mss}$ are calculated with Eqs. (7), (9), (10), (11) and (13). Fatigue parameters, where the stress state is required, have been determined using the extended SSM.

Application of the concept of highly strained volume From the experiments, the numbers of cycles to failure N_f, the highly strained volumes V_ε and the various fatigue parameters $\tilde{\bar{\varepsilon}}_\mathrm{a}^*$, $\tilde{\bar{\varepsilon}}_\mathrm{a}^{*,\mathrm{el}} + \tilde{\bar{\varepsilon}}_\mathrm{a}^{*,\mathrm{pl}}$, P_SWT, ΔW^t and $\Delta W^\mathrm{t}_\mathrm{mss}$ are plotted in three-dimensional graphs with logarithmic scale in Figs. 8, 9, 10 and 11 . In addition to the 3D V_ε-N_f fatigue diagrams, Figs. 8, 9, 10 and 11 show 2D projection views of the fatigue parameters vs. number of cycles to failure N_f for each fatigue parameter. The different specimens (unnotched, notched, bending specimen) are assigned by different markers. The experimental data is approximated with the double power functions

$$[\tilde{\bar{\varepsilon}}_\mathrm{a}^*,\ P_\mathrm{SWT},\ \Delta W^\mathrm{t},\ \Delta W^\mathrm{t}_\mathrm{mss}](N_\mathrm{f},\ V_\varepsilon) = C_1\, N_\mathrm{f}^{d_1} \left(\frac{V_\varepsilon}{\mathrm{mm}^3}\right)^{d_2} \quad (26)$$

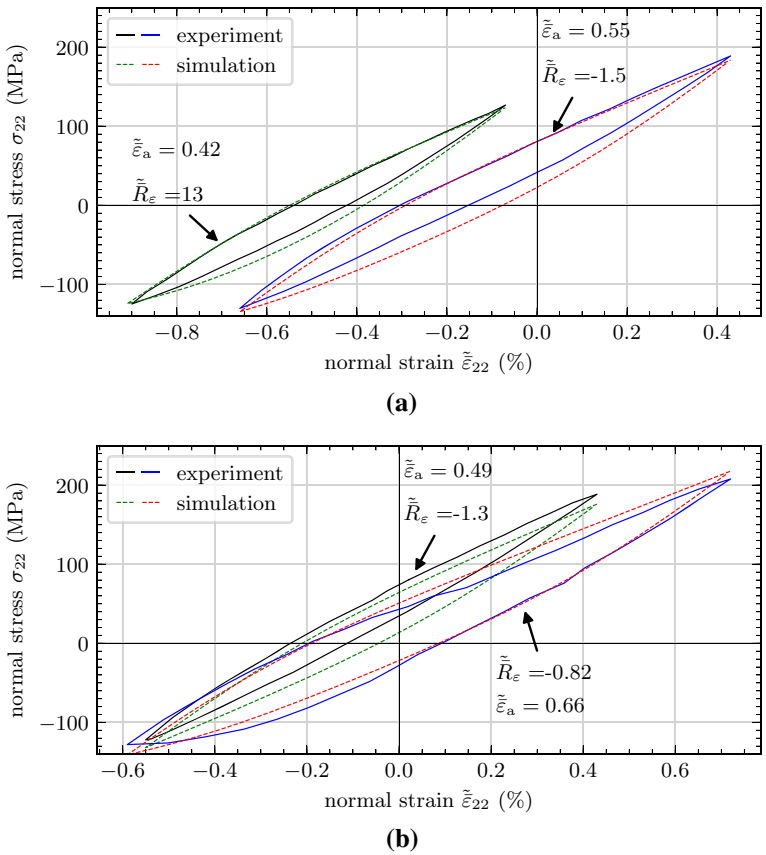

Fig. 7 Comparison between the measured and simulated stress–strain hystereses in the HSR with the mean effective strain ratios: **a** $\tilde{\bar{R}}_\varepsilon = 13$ and $\tilde{\bar{R}}_\varepsilon = -1.5$, **b** $\tilde{\bar{R}}_\varepsilon = -1.3$ and $\tilde{\bar{R}}_\varepsilon = -0.82$

Table 3 Verification of experimentally determined and simulated hystereses with the ratios of the experimentally and simulated maximum stresses σ_{max}, stress amplitudes σ_a, positive elastic ΔW^{+el} and plastic strain energy densities ΔW^{pl} for different mean effective strain ratios $\tilde{\bar{R}}_\varepsilon$

$\tilde{\bar{R}}_\varepsilon$ (-)	$\tilde{\bar{\varepsilon}}$ (%)	$\frac{\sigma_{max\|exp}}{\sigma_{max\|sim}}$ (-)	$\frac{\sigma_{a\|exp}}{\sigma_{a\|sim}}$ (-)	$\frac{\Delta W^{+el}\|_{exp}}{\Delta W^{+el}\|_{sim}}$ (-)	$\frac{\Delta W^{pl}\|_{exp}}{\Delta W^{pl}\|_{sim}}$ (-)
13	0.42	1.04	1.02	1.07	0.711
−1.3	0.49	1.07	1.01	1.15	0.872
−1.5	0.55	1.03	1.00	1.05	0.729
−0.82	0.66	0.97	0.95	0.95	1.03

and

$$[\tilde{\bar{\varepsilon}}_a^{*,el} + \tilde{\bar{\varepsilon}}_a^{*,pl}](N_f,\ V_\varepsilon) = C_1\, N_f^{d_1} \left(\frac{V_\varepsilon}{mm^3}\right)^{d_2} + C_2\, N_f^{d_3} \left(\frac{V_\varepsilon}{mm^3}\right)^{d_4}, \tag{27}$$

wherein the coefficients C_1, C_2 and the exponents $d_1, ..., d_4$ denote material parameters which are used to fit the equations. It should be noted that for the different fatigue parameters the regression coefficients and exponents have different values and units. Finally, the regressions of Eqs. (26) and (27) lead to regression planes for the fatigue parameters $\tilde{\bar{\varepsilon}}_a^*$, P_{SWT}, ΔW^t and ΔW^t_{mss} and to a regression surface for the fatigue parameter $\tilde{\bar{\varepsilon}}_a^{*,el} + \tilde{\bar{\varepsilon}}_a^{*,pl}$, plotted with green color in Figs. 8, 9, 10 and 11. All material parameters for the different fatigue parameters are listed in Table 4. For the nonlinear regression, MATLAB® and its iterative reweighted least-squares algorithm [11,14] is used to determine the material coefficients and exponents.

Verification of the concept of highly strained volume for different fatigue parameters To verify how accurate the nonlinear regression represents the experimental data for the individual fatigue parameters, the coefficient

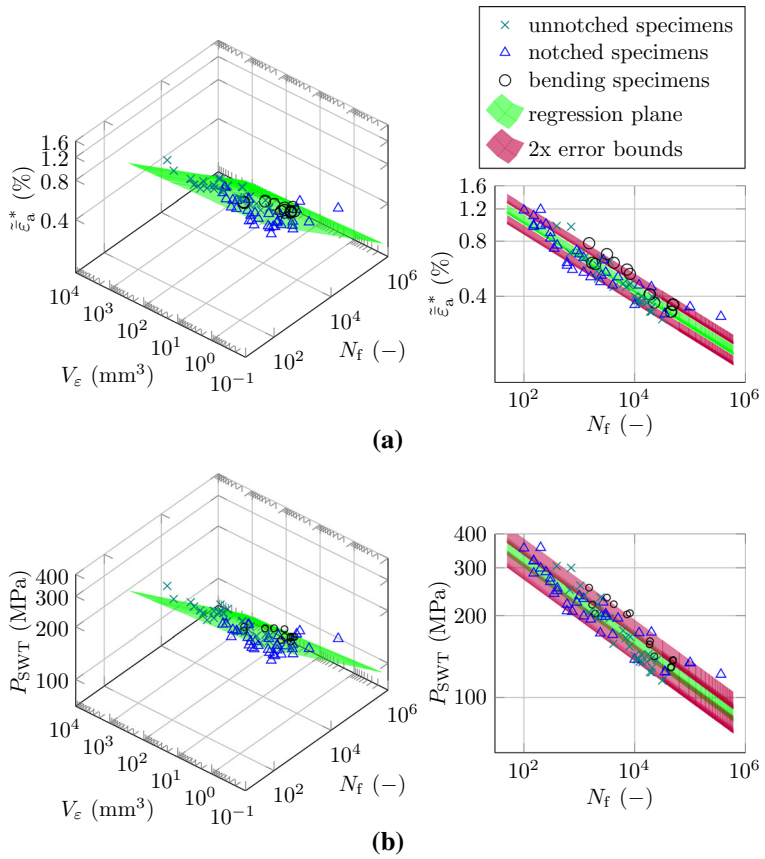

Fig. 8 3D and 2D V_ε-N_f fatigue diagrams including the results from the fatigue tests of the unnotched, notched and bending specimen, the regression planes (green color) and the 2x error bounds (red color). For the fatigue diagrams the fatigue parameters: (a) mean effective principal strain amplitude $\tilde{\tilde{\varepsilon}}_a^*$ and (b) Smith-Watson-Topper P_{SWT} are used

of determination r^2 is calculated. Table 5 lists the coefficient of determination r^2 for the regression surfaces of the different fatigue parameters shown in Figs. 8, 9 and 10.

The best regression is obtained for the fatigue parameter $\tilde{\tilde{\varepsilon}}_a^{*,el} + \tilde{\tilde{\varepsilon}}_a^{*,pl}$ (Fig. 9) with a coefficient of determination of $r^2 = 0.86$ corresponding to a high value, proofing good accuracy. Moreover, the fatigue parameters $\tilde{\tilde{\varepsilon}}_a^*$ and P_{SWT}, plotted in Fig. 8a and b, achieves good accuracy for regression. Table 3 shows that the maximum stress σ_{max} computed with the extended SSM provides accurate results, which is the basis for the good correlation between the regression and the experimental data of both fatigue parameters. The fatigue parameters ΔW^t and ΔW^t_{mss} reveal with $r^2 = 0.82$ (Table 5) the largest discrepancy. As discussed in Sect. 3.3, the computation of the plastic strain energy density ΔW^{pl} results in larger deviations, leading to smaller r^2 values. The use of strain energy density fatigue parameters for fatigue modeling thus requires a more accurate computation of stress–strain hystereses. A further reason for the deviation could be the calculation approach of the positive elastic strain energy density ΔW^{+el}, which considers the mean stress. Roostaei et al. states in [27] that wrought Mg alloys show positive mean stress even during fully reversed strain-controlled tests with strain ratio $R_\varepsilon = -1$. By using their calculation approach of ΔW^{+el}, they improve their fatigue model especially for the load ratio $R = 0.5$. Since the fatigue tests, presented in this paper, were performed at load ratios $R = 2, -\infty$, -1 and -0.5, only small positive mean values result. Thus, the influence of the different calculation approaches for ΔW^{+el} is considered to be small.

The red surfaces in Figs. 8, 9, and 10 represent the 2-times error bounds with respect to the N_f-axis. It can be seen that most experimental data lies between the two two-time error bounds. This demonstrates that the CHεV is well suited for fatigue modeling of wrought Mg alloys, even with different specimen types including stress concentrations, stress gradients, different sizes and different load types.

Verification of the concept of highly strained volume for specific specimen types This paragraph examines the individual influences of the different specimen types. For this purpose the CHεV is applied separately to the

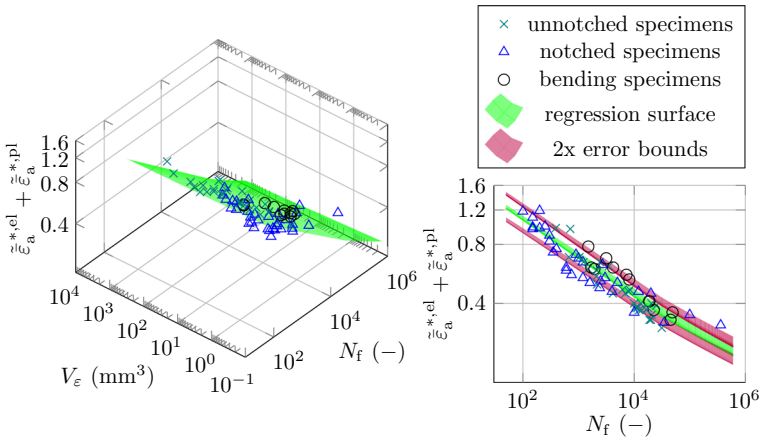

Fig. 9 3D and 2D V_ε-N_f fatigue diagrams including the results from the fatigue tests of the unnotched, notched and bending specimen, the regression surface (green color) and the 2x error bounds (red color). For the fatigue diagrams, the mean effective principal strain amplitude fatigue parameter decomposed in elastic and plastic part $\tilde{\varepsilon}_a^{*,el} + \tilde{\varepsilon}_a^{*,pl}$ is used

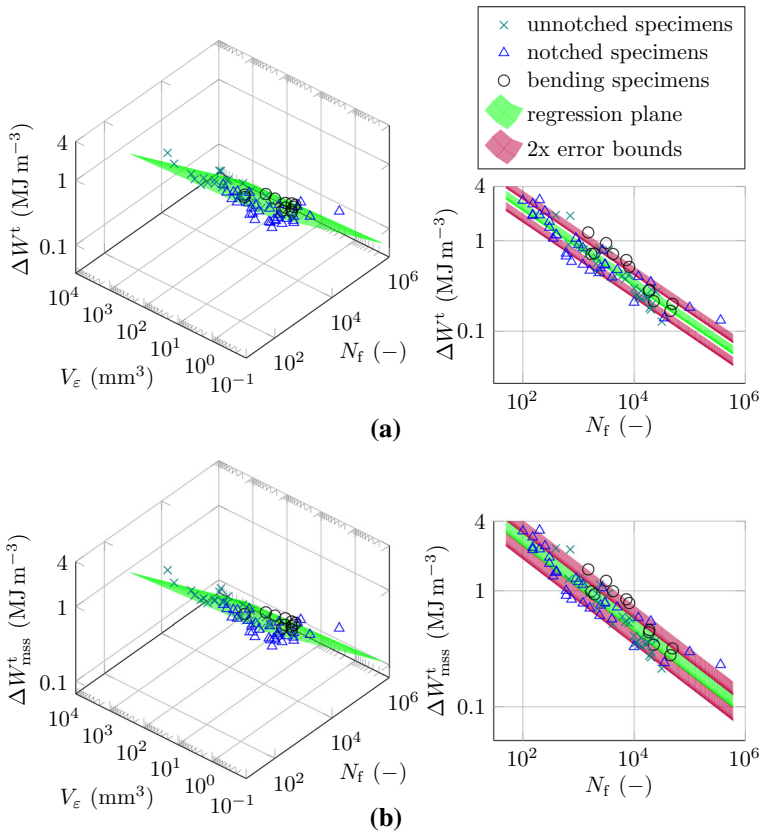

Fig. 10 3D and 2D V_ε-N_f fatigue diagrams including the results from the fatigue tests of the unnotched, notched and bending specimen, the regression planes (green color) and the 2x error bounds (red color). For the fatigue diagrams, the fatigue parameters: (a) total strain energy density ΔW^t and (b) total strain energy density with mean stress sensitivity ΔW^t_{mss} are used

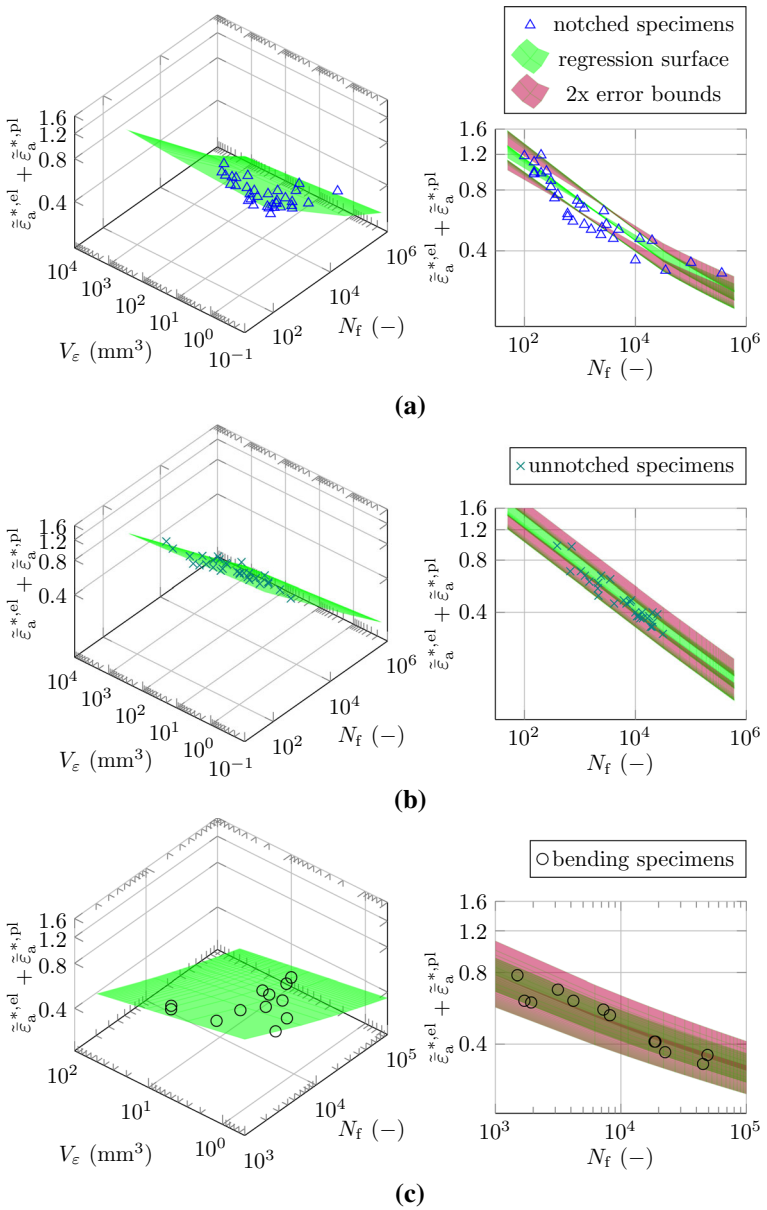

Fig. 11 Verification of the CHεV for the fatigue tests of the: **a** notched specimens ($r^2 = 0.88$), **b** unnotched specimens ($r^2 = 0.89$) and **c** bending specimens ($r^2 = 0.98$). For all of the 3D and 2D V_ε-N_f fatigue diagrams, the fatigue parameter mean effective principal strain amplitude decomposed in elastic and plastic part $\tilde{\tilde{\varepsilon}}_a^{*,el} + \tilde{\tilde{\varepsilon}}_a^{*,pl}$ is used

Table 4 Values for the material parameters for the fatigue parameters, determined with a nonlinear regression analysis which contains all specimen types

Fatigue parameter	C_1	C_2	d_1	d_2	d_3	d_4
$\tilde{\tilde{\varepsilon}}_a^*$	2.57%	–	−0.188	−0.0120	–	–
P_{SWT}	665 MPa	–	−0.149	−0,0150	–	–
ΔW^t	17.4 MJm^{-3}	–	−0.420	−0.0238	–	–
ΔW^t_{mss}	16.2 MJm^{-3}	–	−0.369	−0.0286	–	–
$\tilde{\tilde{\varepsilon}}_a^{*,el} + \tilde{\tilde{\varepsilon}}_a^{*,pl}$	0.914%	2.24%	−0.114	−0.0175	−0.308	0.00578

Table 5 Coefficients of determination r^2 for different fatigue parameters evaluated from the nonlinear regression analysis which contains all specimen types

	$\tilde{\tilde{\varepsilon}}_a^*$	P_{SWT}	ΔW^t	ΔW^t_{mss}	$\tilde{\tilde{\varepsilon}}_a^{*,el} + \tilde{\tilde{\varepsilon}}_a^{*,pl}$
r^2	0.85	0.85	0.82	0.82	0.86

Table 6 Values for the material parameters from the nonlinear regression Eq. (27) for the unnotched, notched, and bending specimen, determined with fatigue parameter $\tilde{\tilde{\varepsilon}}_a^{*,el} + \tilde{\tilde{\varepsilon}}_a^{*,pl}$

Specimen type	C_1 (%)	C_2 (%)	d_1	d_2	d_3	d_4
Unnotched specimens	2.15	2.38	−0.209	−0.0304	−0.308	−0.00787
Notched specimens	0.755	2.19	−0.0906	−0.0336	−0.312	0.0488
Bending specimens	1.09	5.27	−0.118	−0.0742	−0.381	−0.122

Table 7 Coefficients of determination r^2 for the different specimen types, evaluated with the fatigue parameter $\tilde{\tilde{\varepsilon}}_a^{*,el} + \tilde{\tilde{\varepsilon}}_a^{*,pl}$

	Unnotched specimens	Notched specimens	Bending specimens
r^2	0.89	0.88	0.98

fatigue tests of the unnotched, notched, and bending specimens. The verification of the CHεV including all specimen types showed that the fatigue parameter $\tilde{\tilde{\varepsilon}}_a^{*,el} + \tilde{\tilde{\varepsilon}}_a^{*,pl}$ achieved the best regression. Therefore, only the fatigue parameter $\tilde{\tilde{\varepsilon}}_a^{*,el} + \tilde{\tilde{\varepsilon}}_a^{*,pl}$ is used for subsequent fatigue modeling.

Figure 11a–c shows the V_ε-N_f fatigue diagrams containing the experimental data of the fatigue tests of the unnotched, notched and bending specimens, respectively. The regression analysis is carried out on the basis of Eq. (27), with Table 6 listing the determined material coefficients and exponents for the respective specimen types.

Table 7 shows the coefficients of determination r^2 of the regression analyses of the unnotched, notched and bending specimens, where the smallest value is obtained for notched specimens with $r^2 = 0.88$. It was found in [8] that the BTGs that form at notches are relatively small and narrow, which brings the strain field measurement with DIC to its resolution limits. Thus, higher measuring uncertainties cause the slightly lower r^2 value for notched specimens. The best result is obtained for the bending specimens with a coefficient of determination of $r^2 = 0.98$. Figure 11c shows that the values for the highly strained volumes V_ε of the bending specimens cover a smaller range than, e.g., those of the unnotched specimens. The limited variance for this case of the measurement points can be a reason for the good regression. In summary, only small improvements in regressions are achieved for the unnotched and notched specimens by applying the CHεV to only one specific specimen type rather than combining all specimen types in one model. This shows that the CHεV can estimate the lifetime almost as accurately using different specimen types in one model as applying it to a specific specimen type.

5 Conclusions

A method for fatigue modeling of basal textured AZ31B wrought alloy structures is presented, taking into account stress concentrations, stress gradients, different sizes, different types of loading and macroscopic bands of twinned grains (BTGs). The compressive strain in the BTGs is significantly larger compared to the adjacent regions outside the BTGs. Within the BTGs, all investigated fatigue parameters are higher compared to the adjacent regions, which is consistent with the observation that first macroscopic cracks are observed within the BTGs for all specimens. Due to the fact that failure always occurs within the BTGs, only the highly strained regions with high strain amplitudes (HSRA) are considered using the concept of highly strained volume (CHεV).

The main results of this work are summarized in the following items:

- Five fatigue parameters $\tilde{\tilde{\varepsilon}}_a^*$, $\tilde{\tilde{\varepsilon}}_a^{*,el} + \tilde{\tilde{\varepsilon}}_a^{*,pl}$, P_{SWT}, ΔW^t and ΔW^t_{mss} are determined exclusively from the HSRA and evaluated with the CHεV.

- For the fatigue parameters $\tilde{\tilde{\varepsilon}}_a^{*,el} + \tilde{\tilde{\varepsilon}}_a^{*,pl}$, P_{SWT}, ΔW^t and ΔW^t_{mss} stress–strain hystereses must be modeled. Therefore, a stress–strain hysteresis model (SSM) is presented that computes stress–strain hystereses for arbitrary load ratios. Comparisons between experimentally measured and modeled stress–strain hystereses show good agreement.
- In total, the CHεV is applied and evaluated including 30 unnotched, 34 notched and 12 bending specimens using the five fatigue parameters $\tilde{\tilde{\varepsilon}}_a^{*}$, $\tilde{\tilde{\varepsilon}}_a^{*,el} + \tilde{\tilde{\varepsilon}}_a^{*,pl}$, P_{SWT}, ΔW^t and ΔW^t_{mss}. The best regression is achieved for the fatigue parameter $\tilde{\tilde{\varepsilon}}_a^{*,el} + \tilde{\tilde{\varepsilon}}_a^{*,pl}$ with a coefficient of determination $r^2 = 0.86$, demonstrating the aptitude of the CHεV for fatigue modeling of wrought Mg alloys.
- Considering only one specific specimen type in the fatigue model yields only slightly better regressions for the unnotched and notched specimens. The best regression is obtained for the bending specimens with a coefficient of determination of $r^2 = 0.98$. One reason for the good regression can be the limited variance of the highly strained volumes V_ε of the 12 tested bending specimens.

Acknowledgements Open Access funding provided by Projekt DEAL. The authors acknowledge the financial support of the European Regional Development Fund (ERDF) within the funding program INTERREG V-A Programm Österreich-Bayern 2014-2020 in the project 'AB29 - n2m' under the contract number CCI-Nr. 2014TC16RFCB004.

References

1. Albinmousa, J., Jahed, H.: Multiaxial effects on LCF behaviour and fatigue failure of AZ31B magnesium extrusion. Int. J. Fatigue **67**, 103–116 (2014). https://doi.org/10.1016/j.ijfatigue.2014.01.025
2. Ball, E., Prangnell, P.: Tensile-compressive yield asymmetries in high strength wrought magnesium alloys. Scr. Metall. Mater. **31**(2), 111–116 (1994). https://doi.org/10.1016/0956-716X(94)90159-7
3. Cazacu, O., Plunkett, B., Barlat, F.: Orthotropic yield criterion for hexagonal closed packed metals. Int. J. Plast **22**, 1171–1194 (2006). https://doi.org/10.1016/j.ijplas.2005.06.001
4. Dallmeier, J., Denk, J., Huber, O., Saage, H., Eigenfeld, K.: A phenomenological stress–strain model for wrought magnesium alloys under elastoplastic strain-controlled variable amplitude loading. Int. J. Fatigue **80**, 306–323 (2015). https://doi.org/10.1016/j.ijfatigue.2015.06.007
5. Dallmeier, J., Huber, O., Saage, H., Eigenfeld, K.: Uniaxial cyclic deformation and fatigue behavior of AM50 magnesium alloy sheet metals under symmetric and asymmetric loadings. Mater. Des. **70**, 10–30 (2015). https://doi.org/10.1016/j.matdes.2014.12.056
6. Denk, J.: Model for the Fatigue Behavior of Wrought Magnesium Structures Based on Mechanical and Microstructural Characterization. Ph.D. thesis, Paris Lodron University Salzburg (2019). URN urn:nbn:de:bvb:860-opus4-1851
7. Denk, J., Dallmeier, J., Huber, O.: Four-point-bending device for bending moment controlled cyclic reverse loading on plate materials and its application on AZ31B magnesium sheets. Int. J. Fatigue **109**, 49–59 (2018). https://doi.org/10.1016/j.ijfatigue.2017.12.011
8. Denk, J., Dallmeier, J., Huber, O., Saage, H.: The fatigue life of notched magnesium sheet metals with emphasis on the effect of bands of twinned grains. Int. J. Fatigue **98**, 212–222 (2017). https://doi.org/10.1016/j.ijfatigue.2017.01.041
9. Denk, J., Nischler, A., Whitmore, L., Huber, O., Saage, H.: Discontinuous and inhomogeneous strain distributions under monotonic and cyclic loading in textured wrought magnesium alloys. Mater. Sci. Eng. A **764**, 138–182 (2019). https://doi.org/10.1016/j.msea.2019.138182
10. Denk, J., Whitmore, L., Huber, O., Diwald, O., Saage, H.: Concept of the highly strained volume for fatigue modeling of wrought magnesium alloys. Int. J. Fatigue **117**, 283–291 (2018). https://doi.org/10.1016/j.ijfatigue.2018.08.025
11. Dumouchel, W., O'Brien, F.: Integrating a robust option into a multiple regression computing environment. Inst. Math. Appl. **36**, 41 (1991)
12. Ellyin, F., Golos, K.: Multiaxial fatigue damage criterion. J. Eng. Mater. Technol. **110**(1), 63–68 (1988). https://doi.org/10.1115/1.3226012
13. Golos, K., Ellyin, F.: A total strain energy density theory for cumulative fatigue damage. J. Pressure Vessel Technol. **110**(1), 36–41 (1988). https://doi.org/10.1115/1.3265565
14. Holloand, P.W.: Robust regression using iteratively reweighted least-squares. Commun. Stat. **6**(9), 813–827 (1977)
15. Kalatehmollaei, E., Mahmoudi-Asl, H., Jahed, H.: An asymmetric elastic-plastic analysis of the load-controlled rotating bending test and its application in the fatigue life estimation of wrought magnesium AZ31B. Int. J. Fatigue **64**, 33–41 (2014). https://doi.org/10.1016/j.ijfatigue.2014.02.012
16. Koh, S.: Fatigue damage evaluation of a high pressure tube steel using cyclic strain energy density. Int. J. Press. Vessels Pip. **79**(12), 791–798 (2002). https://doi.org/10.1016/S0308-0161(02)00135-7

17. Kuguel, R.: The highly stressed volume of material as a fundamental parameter in the fatigue strength of metal members. Theoretical and Applied Mechanics Report No. 169, Department of Theoretical and Applied Mechanics, University of Illinois, Urbana (1960)
18. Kulekci, M.K.: Magnesium and its alloys applications in automotive industry. Int. J. Adv. Manuf. **39**(9–10), 851–865 (2008). https://doi.org/10.1007/s00170-007-1279-2
19. Lin, Y., Chen, X.M., Liu, Z.H., Chen, J.: Investigation of uniaxial low-cycle fatigue failure behavior of hot-rolled AZ91 magnesium alloy. Int. J. Fatigue **48**, 122–132 (2013). https://doi.org/10.1016/j.ijfatigue.2012.10.010
20. Lou, X., Li, M., Boger, R., Agnew, S., Wagoner, R.: Hardening evolution of AZ31B Mg sheet. Int. J. Plast **23**(1), 44–86 (2007). https://doi.org/10.1016/j.ijplas.2006.03.005
21. Masoumi, M., Zarandi, F., Pekguleryuz, M.: Microstructure and texture studies on twin-roll cast AZ31 (Mg-3 wt%Al-1 wt%Zn) alloy and the effect of thermomechanical processing. Mater. Sci. Eng. A **528**(3), 1268–1279 (2011). https://doi.org/10.1016/j.msea.2010.10.003
22. Mordike, B.L., Ebert, T.: Magnesium-properties-applications-potential. Mater. Sci. Eng. A **302**(1), 37–45 (2001). https://doi.org/10.1016/S0921-5093(00)01351-4
23. Park, S.H., Hong, S.G., Lee, B.H., Bang, W., Lee, C.S.: Low-cycle fatigue characteristics of rolled Mg–3Al–1Zn alloy. Int. J. Fatigue **32**(11), 1835–1842 (2010). https://doi.org/10.1016/j.ijfatigue.2010.05.002
24. Roostaei, A., Jahed, H.: Multiaxial cyclic behaviour and fatigue modelling of AM30Mg alloy extrusion. Int. J. Fatigue **97**, 150–161 (2017). https://doi.org/10.1016/j.ijfatigue.2016.12.037
25. Roostaei, A.A., Jahed, H.: A cyclic small-strain plasticity model for wrought Mg alloys under multiaxial loading: numerical implementation and validation. Int. J. Mech. Sci. **145**, 318–329 (2018). https://doi.org/10.1016/j.ijmecsci.2018.07.024
26. Roostaei, A.A., Ling, Y., Jahed, H., Glinka, G.: Applications of Neuber's and Glinka's notch plasticity correction rules to asymmetric magnesium alloys under cyclic load. Theoret. Appl. Fract. Mech. **105**, 102431 (2020). https://doi.org/10.1016/j.tafmec.2019.102431
27. Roostaei, A.A., Pahlevanpour, A., Behravesh, S.B., Jahed, H.: On the definition of elastic strain energy density in fatigue modelling. Int. J. Fatigue **121**, 237–242 (2019). https://doi.org/10.1016/j.ijfatigue.2018.12.011
28. Shih, T., Liu, W., Chen, Y.: Fatigue of as-extruded AZ61A magnesium alloy. Mater. Sci. Eng. A **325**(1), 152–162 (2002). https://doi.org/10.1016/S0921-5093(01)01411-3
29. Ucuncuoglu, S., Ekerim, A., Secgin, G., Duygulu, O.: Effect of asymmetric rolling process on the microstructure, mechanical properties and texture of AZ31 magnesium alloys sheets produced by twin roll casting technique. J. Magnes. Alloys **2**(1), 92–98 (2014). https://doi.org/10.1016/j.jma.2014.02.001
30. Wagner, L., Hilpert, M., Wendt, J., Küster, B.: On Methods for Improving the Fatigue Performance of the Wrought Magnesium Alloys AZ31 and AZ80. Mater. Sci. Forum **419**, 93–102 (2003). https://doi.org/10.4028/www.scientific.net/MSF.419-422.93
31. Wu, L., Agnew, S., Ren, Y., Brown, D., Clausen, B., Stoica, G., Wenk, H., Liaw, P.: The effects of texture and extension twinning on the low-cycle fatigue behavior of a rolled magnesium alloy, AZ31B. Mater. Sci. Eng. A **527**(26), 7057–7067 (2010). https://doi.org/10.1016/j.msea.2010.07.047
32. Zhang, P., Lindemann, J., Leyens, C.: Influence of shot peening on notched fatigue strength of the high-strength wrought magnesium alloy AZ80. J. Alloy. Compd. **497**(1), 380–385 (2010). https://doi.org/10.1016/j.jallcom.2010.03.079